LETTERS

Shear heating as the origin of the plumes and heat flux on Enceladus

F. Nimmo[1], J. R. Spencer[2], R. T. Pappalardo[3] & M. E. Mullen[4]

Enceladus, a small icy satellite of Saturn, has active plumes jetting from localized fractures ('tiger stripes') within an area of high heat flux near the south pole[1–4]. The plume characteristics[1] and local high heat flux[2] have been ascribed either to the presence of liquid water within a few tens of metres of the surface[1], or the decomposition of clathrates[5]. Neither model addresses how delivery of internal heat to the near-surface is sustained. Here we show that the most likely explanation for the heat[2] and vapour production[6,7] is shear heating by tidally driven lateral (strike-slip) fault motion[1,8,9] with displacement of ~0.5 m over a tidal period. Vapour produced by this heating may escape as plumes through cracks reopened by the tidal stresses[10]. The ice shell thickness needed to produce the observed heat flux is at least 5 km. The tidal displacements required imply a Love number of $h_2 > 0.01$, suggesting that the ice shell is decoupled from the silicate interior by a subsurface ocean. We predict that the tiger-stripe regions with highest relative temperatures will be the lower-latitude branch of Damascus, Cairo around 60° W longitude and Alexandria around 150° W longitude.

Mid-infrared observations of the tiger stripes show spatially varying temperature anomalies with mean temperatures a few kelvin higher than the background, and also require regions a few hundred metres wide with temperatures up to at least 150 K (ref. 2). The total heat flow for the region south of 65° S is 3.9–7.7 GW (ref. 2). Stellar occultation and mass spectrometer data suggest that the vapour plume mass flux is 120–180 kg s^{-1} (refs 6, 7). The mass of solid ice grains relative to water vapour in the plume has been used to argue that the plume is generated by shallow boiling liquid water[1]. Alternatively, clathrate decomposition may be able to produce the observed plume[5]. However, neither of these models addresses how heat is transported to the near-surface to sustain these putative processes.

Lateral (strike-slip) motion has previously been inferred for Jupiter's moon Europa[11], which probably possesses a subsurface ocean[12]. Such motion would occur as a result of the time-varying orientation of tidal stresses on that body[13], and may result in localized heating due to friction or viscous dissipation[8]. Faults in the polar regions of Enceladus will experience stresses driving strike-slip motion for part of each tidal cycle[13,14] (see Supplementary Information). According to ref. 15, the mean shear velocity on an individual fault driven by these tidal stresses is given by $u = (\mathrm{d}\varepsilon/\mathrm{d}t)d \approx (4 \times 10^{-5} h_2)$ m s^{-1} (see Supplementary Information). Here d is the distance between faults (assumed to be 30 km for the tiger stripes[1]), h_2 is a dimensionless (Love) number that depends on the satellite's internal structure, and $\mathrm{d}\varepsilon/\mathrm{d}t$ is the mean diurnal tidal strain rate. For a uniform body that lacks significant rigidity (h_2 approaching 2.5) and fault friction, the shear velocity will be of the order of 10^{-4} m s^{-1}. The shear velocity controls the shear heating rate. The presence of fault friction, an elastic ice shell, or a silicate interior will reduce h_2 and the shear velocity by as much as several orders of magnitude[16] (see below).

To calculate the thermal consequences of this strike-slip motion, we use an approach[8,9] in which a single shear zone generates local heating in a floating ice shell. We adopt a nominal conductive ice layer thickness of 24 km (compare with ref. 17), comparable to the tiger-stripe spacing, which may be underlain by a convecting icy interior[18] and a global subsurface ocean or a localized sea. The shearing is accomplished by motion on a discrete vertical fault surface at shallow depths where the ice is cold and brittle, and by ductile motion across a broader shear zone at greater depths. The transition depth between brittle and ductile deformation is calculated in a self-consistent manner[9], and the resulting equilibrium temperature structure is derived. The surface temperature is calculated based on the subsurface and radiative heat fluxes (see Supplementary Information).

The energy generated by shearing will be partitioned principally between heating and vapour sublimation[19]. We adopt a dimensionless free parameter α to describe this partitioning, where $\alpha = 0$ implies that all the energy goes into vapour production, and $\alpha = 1$ means all the energy goes into heating. To provide a zeroth-order description of the likely vapour transport processes (see Supplementary Information) we solve the diffusion equation[20,21] $\partial\rho_v/\partial t = D\nabla^2\rho_v + (1-\alpha)H/L\phi$ to the steady state, where ρ_v is the pore vapour density, D and L are the (temperature-dependent) diffusivity[20] and latent heat of sublimation[22], respectively, H is the total volumetric heat production in the ice calculated for the steady-state temperature distribution, and ϕ is the porosity[21]. In steady-state the vapour escape rate is independent of the permeability structure assumed (see Supplementary Information). Although we do not consider the timing or details of volatile release, vapour escape is probably mainly through the brittle shear zone that is opened and closed by the periodic tidal stresses[10].

Figure 1 shows that the temperatures and temperature gradients near the strike-slip zone are significantly increased as a result of the brittle and viscous heating when the shear velocity is 8×10^{-6} m s^{-1} (~0.5 m slip per tidal cycle; $h_2 \approx 0.2$) and $\alpha = 0.1$. The brittle layer thickness is locally reduced to 4 km along the fracture, implying that peak shear stresses of ~100 kPa are required to cause motion, comparable to the tidal shear stresses expected for $h_2 \approx 0.2$ (see Supplementary Information).

Because the bulk of the energy is partitioned into vapour production, the total conductive heat flow (0.95 GW for a total fault length of 500 km; ref. 1) and maximum surface temperature increase (1.1 K) are smaller than the infrared observations[2]. On the other hand, the vapour production rate of ~2,000 kg s^{-1} is ten times larger than the inferred plume flux[7]. We propose that the infrared signature is the result of latent heat released by local recondensation of ~90% of the vapour in cold, near-surface porous ice around the shear zone[5],

[1]Department of Earth and Planetary Sciences, University of California Santa Cruz, 1156 High Street, Santa Cruz, California 95064, USA. [2]Department of Space Studies, Southwest Research Institute, 1050 Walnut Street, Boulder, Colorado 80304, USA. [3]Planetary Science and Life Detection Section, Jet Propulsion Laboratory, California Institute of Technology, Mail Stop 183-301, Pasadena, California 91109, USA. [4]Department of Astrophysical and Planetary Sciences, Campus Box 391, University of Colorado, Boulder, Colorado 80309-0391, USA.

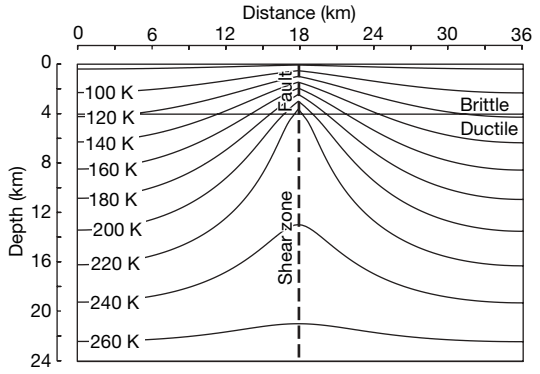

Figure 1 | Shear heating model. Cross-section of steady-state temperature structure (in kelvin) for a shear velocity of 8×10^{-6} m s^{-1} (implying a Love number $h_2 \approx 0.2$; see text) and $\alpha = 0.1$ (implying that 90% of the dissipation goes into vapour production rather than temperature increases). The bold dashed line represents a vertical fault along which lateral shear occurs (perpendicular to the page); the brittle layer thickness at the shear zone is calculated self-consistently[9]. This model produces 0.95 GW of conductive heat flow (assuming a 500 km length) and a total vapour production rate of 2,160 kg s^{-1}; recondensation of the vapour would add a further 6 GW of heat. The ice viscosity is temperature-dependent (ref. 27, see Supplementary Information). Calculations assume coefficient of friction $f = 0.3$, $g = 0.11$ m s^{-2}, ice density $\rho = 930$ kg m^{-3}, ice reference viscosity 10^{13} Pa s, thermal conductivity 3 W m^{-1} K^{-1}, grid spacing 0.3 km (horizontal) and 0.2 km (vertical), surface temperature in absence of subsurface heating 75 K (ref. 2); other parameters identical to ref. 8. The results are relatively insensitive to changes in viscosity or shell thickness (see Supplementary Information).

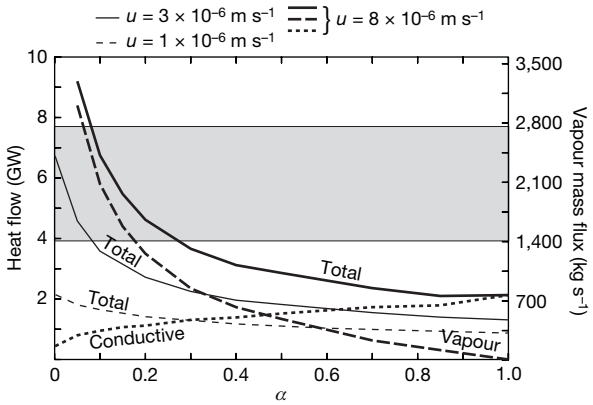

Figure 2 | Heat flow and vapour flux as a function of shear velocity *u* and parameter α. The free parameter α controls what fraction of energy dissipated goes into vapour production. The vapour curve refers to both vapour mass flux and heat flow; other curves refer to heat flow only. Vapour production is calculated using the Methods described in the Supplementary Information. Vapour-driven heat flow is calculated by assuming that all the vapour recondenses with a latent heat of 2.8 MJ kg^{-1}. Conductive heat flow is obtained by integrating the surface heat flux across the computational domain. Total tiger-stripe length is assumed to be 500 km and shell thickness is 24 km. Increased vapour production produces a colder shear zone and allows the brittle layer to extend to greater depths, resulting in an overall increase in heat production. The shaded zone indicates the surface heat flow deduced from Cassini observations[2]. With a 24-km-thick shell, a shear velocity of 10^{-6} m s^{-1} ($h_2 = 0.02$) is insufficient to match the observations. A conservatively thick (81 km) shell requires $h_2 > 0.01$.

while the remaining vapour escapes to form the observed plumes. Recondensation of 1,800 kg s^{-1} vapour over a shallow subsurface zone 500 m wide and 500 km long results in a heat flow of 5 GW and an equivalent surface temperature of 137 K, consistent with the infrared observations[2]. Heating and consequent ice grain growth due to this recondensation is also a plausible explanation of the greater inferred grain size at the tiger stripes[1,23].

The modelled flux-weighted temperature of the vapour entering the shear zone is ~175 K (root-mean-square thermal velocity ~500 m s^{-1}). Particles escaping the shear zone upwards are likely to be collimated, resulting in a vertical velocity comparable to the thermal velocity, but much larger than the horizontal velocity. The thermal velocity we obtain is thus consistent with modelling of the Cassini vapour observations[7]. The Cassini-derived particle ejection rate[1] was about 1/40th of the estimated 150 kg s^{-1} gas production rate[7] observed four months earlier. Because most of the ~2,000 kg s^{-1} of vapour generated in our model is assumed to condense near the surface, the entrainment in the plume of a small fraction (<1%) of the condensing solids is plausible without invoking near-surface liquid water.

Figure 2 shows that our results are sensitive to the shear velocity and value for α adopted. Greater vapour production (smaller α) results in less heating of the ice, an increased depth of brittle deformation, and a greater overall power output. A shear velocity of 10^{-6} m s^{-1} results in a total power output less than that of the

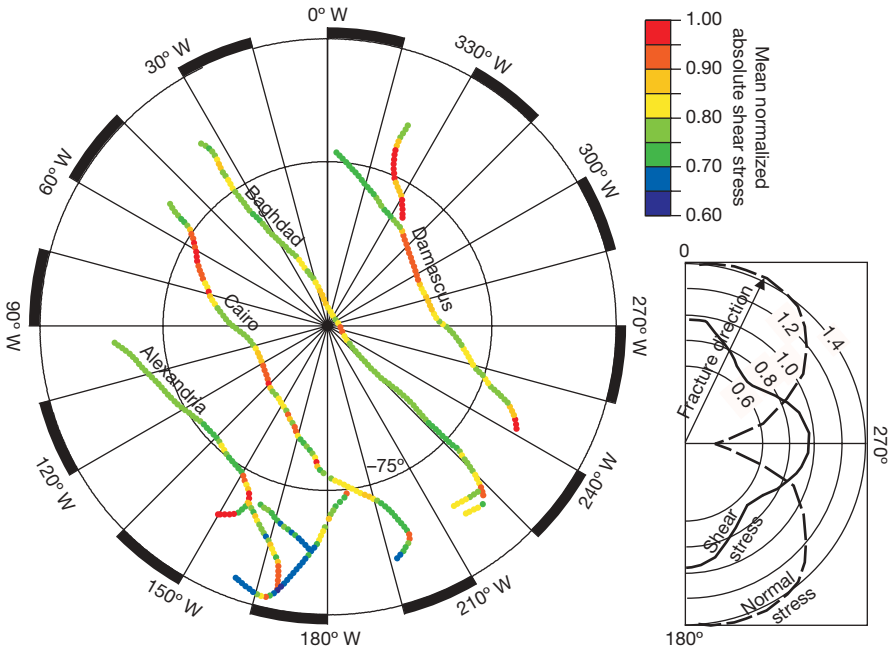

Figure 3 | Predicted tiger-stripe stresses. Plotted is a polar stereographic projection of Enceladus tiger stripes and related structures south of 64° S. Colours indicate mean absolute shear stress (averaged over one tidal cycle), resolved onto the local tiger-stripe orientation and normalized to the maximum value (see Supplementary Information for further details). Areas with higher resolved shear stresses will undergo greater long-term shear heating and vapour production. For brittle heating, the long-term heat production rate will be linearly proportional to the plotted shear stress. Thus, areas with higher stress will show higher temperatures. Cairo is a particularly good target for future Cassini observations because of the predicted variations in temperature along its length. The inset plots the normalized resolved shear and normal stresses as a function of fracture orientation for a fracture located at 70° S, 165° W. Circular contours give normalized stress magnitudes. Normal stresses are maximized on fractures oriented close to the direction of 0° or 180°; shear stresses are maximized on fractures oriented in the direction of 0°, 90°, 180° or 270°.

infrared observations. For a conservatively thick (81 km) ice shell, the same constraint results in a lower bound on h_2 of 0.01.

We have simplified or neglected many details of the vapour sublimation and transport mechanisms, such as their effect on the temperature[19,24] and porosity structure[21], and the potential for time-variable transport and release[6,10]. Nonetheless, Fig. 2 shows that shear heating can generate enough power and vapour to account for the observations. For the shell properties we assume, shell thicknesses in excess of 5 km are required to match the observed heat flow (Supplementary Information).

Different tiger stripes will experience different rates of long-term heating, due to the spatial variation in tidal stresses and the tiger stripe orientation. Figure 3 plots the time-averaged absolute shear stress resolved onto the local tiger stripe orientation and normalized to the maximum shear stress (Supplementary Information). The shear velocity, and thus the long-term heating rate, will be proportional to this quantity if brittle heating dominates[8,9]. Despite their variable spatial resolution, some existing thermal infrared observations[2] support our model. In particular, the two branches of Damascus show a temperature variation consistent with the prediction, and Cairo has a hotspot at about 120° longitude, as predicted. On the other hand, Baghdad temperatures are higher than expected.

The inset in Fig. 3 shows how the resolved stresses vary as a function of fracture azimuth for near-polar fractures. The current orientation of the tiger stripes results in near-maximum normal stresses, suggesting they may have initiated as tensile cracks from contemporary diurnal tides.

In our shear-heating model, the shear velocities required to match the observations imply a Love number $h_2 > 0.01$. A global subsurface ocean decouples the ice shell from the silicate interior and permits larger shear velocities and greater tidal heating[16,17]. Figure 4 shows the Love number h_2 as a function of ice shell viscosity for spherically symmetric models with and without a subsurface ocean. A model with a global subsurface ocean can reproduce the shear velocities required for reasonable assumptions of ice viscosity. The shear heating model is also consistent with reorientation of the south polar region owing to density anomalies in a relatively thick ice shell; the presence of an ocean argues against that density anomaly being located in a decoupled rocky core[25]. In the absence of an ocean, unrealistically low ice shell (or silicate mantle) viscosities are required. To generate the shear velocities required, it seems likely that Enceladus has a subsurface ocean, either global or possibly localized[26], beneath a thick ice shell.

Our hypothesis suggests that permanent strike-slip offsets might be present[13] and potentially observable, although the cyclical nature of the shearing could result in negligible net strike-slip offset. More important, the regions with the highest relative temperatures are predicted to be the lower-latitude branch of Damascus, Cairo around 60° W longitude, and Alexandria around 150° W longitude (Fig. 3).

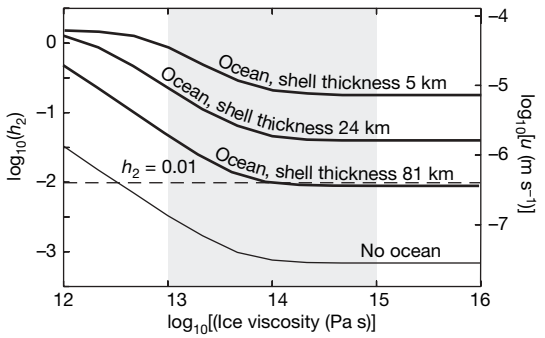

Figure 4 | Effect of interior structure on mean shear velocity. Love numbers h_2 and resulting mean shear velocities u ($= 4 \times 10^{-5} h_2$ m s^{-1}; see text) for models of a spherically symmetric Enceladus with and without an interior ocean are plotted as a function of ice shell viscosity. The shaded region denotes the probable range in viscosity for a convecting ice shell with a grain size of 0.1–10 mm and a temperature of 250–270 K (refs 27, 28); the dashed line plots the estimated lower bound on h_2 (see text). Calculations were carried out using the method of ref. 16 and using parameters similar to those in ref. 25. The silicate core has a radius of 161 km, density of 3,500 kg m^{-3}, a rigidity of 100 GPa and viscosity of 10^{21} Pa s. The ocean (where present) plus ice shell have a combined thickness of 91 km. The ice shell has a density and rigidity of 950 kg m^{-3} and 3 GPa, respectively, a constant assumed viscosity, and a thickness of 5, 24 or 81 km. The silicate mantle viscosity would have to be reduced to an unrealistically low 10^{14} Pa s or less to allow any significant increase in deformation of the model lacking an ocean. Including the effect of the conductive ice lid would further reduce the value of h_2. For large ice viscosities the body behaves in a purely elastic fashion and h_2 is independent of viscosity.

Received 8 December 2006; accepted 22 March 2007.

1. Porco, C. C. *et al.* Cassini observes the active south pole of Enceladus. *Science* **311,** 1393–1401 (2006).
2. Spencer, J. R. *et al.* Cassini encounters Enceladus: background and the discovery of a south polar hot spot. *Science* **311,** 1401–1405 (2006).
3. Spahn, F. *et al.* Cassini dust measurements at Enceladus and implications for the origin of the E ring. *Science* **311,** 1416–1418 (2006).
4. Hansen, C. J. *et al.* Enceladus' water vapour plume. *Science* **311,** 1422–1425 (2006).
5. Kieffer, S. W. *et al.* A clathrate reservoir hypothesis for Enceladus' south polar plume. *Science* **314,** 1764–1766 (2006).
6. Waite, J. H. *et al.* Cassini ion and neutral mass spectrometer: Enceladus plume composition and structure. *Science* **311,** 1419–1422 (2006).
7. Tian, F., Stewart, A. I. F., Toon, O. B., Larsen, K. M. & Esposito, L. W. Monte Carlo simulations of the water vapor plumes on Enceladus. *Icarus* (in the press).
8. Nimmo, F. & Gaidos, E. Thermal consequences of strike-slip motion on Europa. *J. Geophys. Res.* **107,** 5021, doi:10.1029/2000JE001476 (2002).
9. Prockter, L. M., Nimmo, F. & Pappalardo, R. T. A shear heating origin for ridges on Triton. *Geophys. Res. Lett.* **32,** L14202, doi:10.1029/2005GL022832 (2005).
10. Hurford, T. A., Helfenstein, P., Hoppa, G. V., Greenberg, R. & Bills, B. G. Eruptions arising from tidally controlled periodic openings of rifts on Enceladus. *Nature* doi:10.1038/nature05821 (this issue).
11. Hoppa, G. *et al.* Distribution of strike-slip faults on Europa. *J. Geophys. Res.* **105,** 22617–22627 (2000).
12. Zimmer, C., Khurana, K. K. & Kivelson, M. G. Subsurface oceans on Europa and Callisto: constraints from Galileo magnetometer observations. *Icarus* **147,** 329–347 (2000).
13. Hoppa, G., Tufts, B. R., Greenberg, R. & Geissler, P. Strike-slip faults on Europa: global shear patterns driven by tidal stress. *Icarus* **141,** 287–298 (1999).
14. Helfenstein, P. & Parmentier, E. M. Patterns of fracture and tidal stresses on Europa. *Icarus* **53,** 415–430 (1983).
15. Greenberg, R. *et al.* Tectonic processes on Europa: tidal stresses, mechanical response and visible features. *Icarus* **135,** 64–78 (1998).
16. Moore, W. B. & Schubert, G. The tidal response of Europa. *Icarus* **147,** 317–319 (2000).
17. Ross, M. N. & Schubert, G. Viscoelastic models of tidal heating on Enceladus. *Icarus* **78,** 90–101 (1989).
18. Squyres, S. W., Reynolds, R. T., Cassen, P. M. & Peale, S. J. The evolution of Enceladus. *Icarus* **53,** 319–331 (1983).
19. Komle, N. I. *et al.* Temperature evolution and vapour pressure build-up in porous ices. *Planet. Space Sci.* **40,** 1311–1323 (1992).
20. Clifford, S. M. & Hillel, D. The stability of ground ice in the equatorial region of Mars. *J. Geophys. Res.* **88,** 2456–2474 (1983).
21. Schorghofer, N. & Aharonson, O. Stability and exchange of subsurface ice on Mars. *J. Geophys. Res.* **110,** E05003, doi:10.1029/2004JE002350 (2005).
22. Cowan, J. J. & A'Hearn, M. F. Vaporization of comet nuclei: light curves and life times. *Moon Planets* **21,** 155–171 (1979).
23. Brown, R. H. *et al.* Compsition and physical properties of Enceladus' surface. *Science* **311,** 1425–1428 (2006).
24. Espinasse, S., Klinger, J., Ritz, C. & Schmitt, B. Modeling of the thermal behaviour and of the chemical differentiation of cometary nuclei. *Icarus* **92,** 350–365 (1991).
25. Nimmo, F. & Pappalardo, R. T. Diapir-induced reorientation of Saturn's moon Enceladus. *Nature* **441,** 614–616 (2006).
26. Collins, G. C. & Goodman, J. C. Enceladus's south polar sea. *Icarus* (in the press).
27. Goldsby, D. L. & Kohlstedt, D. L. Superplastic deformation of ice: Experimental observations. *J. Geophys. Res.* **106,** 11017–11030 (2001).
28. Pappalardo, R. T. *et al.* Geological evidence for solid-state convection in Europa's ice shell. *Nature* **391,** 365–368 (1998).

Supplementary Information is linked to the online version of the paper at www.nature.com/nature.

Acknowledgements We thank D. Gleeson and Z. Crawford for their efforts. This work was funded by NASA's Planetary Geology and Geophysics and Outer Planets Research programmes.

Author Information Reprints and permissions information is available at www.nature.com/reprints. The authors declare no competing financial interests. Correspondence and requests for materials should be addressed to F.N. (fnimmo@es.ucsc.edu).